

Data Augmentation for Histopathological Images Based on Gaussian-Laplacian Pyramid Blending

Steve Tsham Mpinda Ataky*, Jonathan de Matos*[§], Alceu de S. Britto Jr.^{†§}
Luiz E. S. Oliveira[‡] and Alessandro L. Koerich*

*École de Technologie Supérieure, Université du Québec, Montréal, QC, Canada

Email: steve.ataky@nca.ufma.br, alessandro.koerich@etsmtl.ca

[§]State University of Ponta Grossa (UEPG), Ponta Grossa, PR, Brazil

Email: jonathan@uepg.br

[†]Pontifical Catholic University of Paraná, Curitiba, PR, Brazil

Email: alceu@ppgia.pucpr.br

[‡]Federal University of Paraná, Curitiba, PR, Brazil

Email: luiz.oliveira@ufpr.br

Abstract—Data imbalance is a major problem that affects several machine learning algorithms. Such problems are troublesome because most of the learning algorithms attempts to optimize a loss function based on error measures that do not take into account the data imbalance. Accordingly, the learning algorithm simply generates a trivial model that is biased toward predicting the most frequent class in the training data. Data augmentation techniques have been used to mitigate the data imbalance problem. However, in the case of histopathologic images (HIs), low-level as well as high-level data augmentation techniques still present performance issues when applied in the presence of inter-patient variability; whence the model tends to learn color representations, which are in fact related to the stain process. In this paper, we propose an approach capable of not only augmenting HIs database but also distributing the inter-patient variability by means of image blending using Gaussian-Laplacian pyramid. The proposed approach consists in finding the Gaussian pyramids of two images of different patients and finding the Laplacian pyramids thereof. Afterwards, the left half of one image and the right half of another are joined in each level of Laplacian pyramid, and from the joint pyramids, the original image is reconstructed. This composition, resulting from the blending process, combines stain variation of two patients, avoiding that color misleads the learning process. Experimental results on the BreakHis dataset have shown promising gains vis-à-vis the majority of traditional techniques presented in the literature.

Index Terms—histopathologic images, data augmentation, Gaussian-Laplacian pyramids, images blending

I. INTRODUCTION

Cancer is a global health problem and can be the greatest barrier to the long life expectancy worldwide in the 21st century [1]. Due to its impact on life expectancy and life quality, the efforts to combat the disease are stabilizing the mortality in high-income countries. The aforementioned efforts are focused on reducing risk factors like smoking, overweight, physical inactivity and promote early diagnosis and treatment. Breast cancer is the most prevalent cancer type among women in 140 out of 184 countries according as stated by [2]. Its detection usually starts based on the self-examination and periodic

mammography. These exams can identify lumps which will be examined in detail by ultrasound, computed tomography (CT) or magnetic resonance imaging (MRI). When some characteristics that can point to a malignant tumor are detected by imaging exams, the final step is the biopsy, which is considered the gold-standard in the diagnosis process because it provides the most accurate diagnosis of the tumor type. The diagnosis procedure should be fast because some malignant tumors grow very fast and have high metastasis probability.

Biopsies are a complex diagnosis tool, requiring the acquisition of material (e.g. fine-needle aspiration or open surgical biopsy), tissue treatment (slicing, staining and slide preparation) and analysis. The analysis requires an experienced pathologist besides being time-consuming and subject to inter and intra-observer issues [3]. The variance in the results can be due to the pathologist experience or the hematoxylin and eosin (H&E) staining color differences, which may be related to stain manufacturers, storage age and temperature. Computer-aided diagnosis (CAD) systems can help in such analysis by adding an extra opinion to the pathologist decision. CAD systems can rely on histopathologic images (HIs), which are obtained from tissue slides scanning, to make decisions about tumor characteristics, e.g. benign or malignant [4].

The automatic classification of HIs is a challenging problem in machine learning because HIs do not have the same structured aspect as macroscopic images, like people's faces, cars, animals or traffic signs. One structure that is important in HIs is the nucleus. In images stained with H&E, hematoxylin highlights the nucleus with a blueish color and eosin highlights the cytoplasm and extracellular matrix in pink. The importance of the nucleus in tumor diagnosis is related to their quantity and their format. When a region presents a highly abnormal amount of nucleus, this can be an indication of excessive cell multiplication, being a strong sign of a tumor. The format of the nucleus may also represent a signal of a tumor, this is called nucleus pleomorphism. Although blue and pink are the colors expected in H&E stained slides, it is common to face

differences in intensity, saturation, and hue in the HIs.

When analyzing an HI dataset, it is possible to note the differences, which are more evident when looking into images of different patients. Slides from different patients may have used other stain brands or faced variations during the whole process. The pathologist can understand this variation easily due to its expertise in looking at the important HI features. However, color variations between patients may introduce a bias in the classification by machine learning algorithms. The image color of one patient does not vary because the staining process was the same, but the inter-patient color, to the same tumor type, may be different. It is also possible to exist images of different patients with similar color, even with one being benign and another a malignant tumor. Color normalization [5], [6] may help minimize the color bias and it requires a target image, used as a reference to guide the normalization algorithm. Choosing the target image is a complex task, which may cause some images to lose important characteristics when trying to mimic another image color. Furthermore, the classification result is closely related to such a reference image.

Another aspect related to the classification of HIs is the number of images available to train a machine learning model. One fact that made possible the latest evolution in machine learning is the development of deep learning. These methods have been achieved impressive performance mainly in daily life problems related to images, but they require datasets such as the ImageNet dataset [7], which encompasses millions of images. HI datasets are usually small because analyzing and labeling HIs is expensive and requires experienced pathologists. Low data scenarios are not adequate for deep learning because it produces large models with millions of parameters, which leads to over-fitting problems. The data augmentation has been actively used to circumvent this issue. Besides that, HI datasets can also suffer from the data imbalance due to tumor occurrence rate and the biopsy priorities. As the biopsy procedure is expensive and time-consuming, it is usually carried out when malignant tumors are previously diagnosed through non-invasive exams. On the other hand, biopsy is not required when most of the benign tumors are detected. Therefore, it is common in the case of breast cancer biopsies to have a higher number of malignant HIs than benign HIs. Such an imbalance impacts on machine learning algorithms, but there are some approaches that attempt to circumvent this problem.

The main contributions of this paper are: (i) a new data augmentation method that simultaneously provides color normalization and augmentation; (ii) a method to improve data classification by reducing the data imbalance; (iii) the advantages of using a texture convolutional neural network for HI classification. This paper is organized as follows: Section II presents related works found in literature to data augmentation and data balancing, as well as their advantages and limitations. Section III briefly describes Gaussian-Laplacian pyramids, pyramid blending and presents the proposed approach for data augmentation. Section IV describes the experimental setup

used in this work. Results and conclusions are reported in Sections V and VI, respectively.

II. RELATED WORKS

One way to circumvent the over-fitting problems owing to the small and imbalanced dataset problem is by means of data augmentation, which has been exploited in many articles related to HI, usually applying low-level transformation such as flip and rotation [8]–[11]. Notwithstanding, based on the principle that transformations are motion geometry, the shape/object created during a transformation is an image of the original one. The rotation, which consists of turn of an image makes a congruent image of the original, but facing another direction. The flip, likewise, creates a congruent mirror image of the original one. In both cases, the number of images increases but the heterogeneity in terms of texture is preserved. In other word, considering HIs, low-level transformation solve the over-fitting but in terms of the number of images, not in terms of inter-patient variability.

Another strategy for data augmentation that has been used with HIs is patching [12]–[14]. In this method, an image is divided into a number of patches (overlapped or not), thus from one sample n samples are generated. Regardless of the gain in terms of data, some patches may contain no meaningful information, in light of their size, the magnification of the original image as well as their location in the original images. By the same token, there are works that also used data augmentation employing color disturbance [15], [16]. These works contributed not only to increase the number of images but also in removing the color bias.

Concerning the data imbalance due to tumor occurrence rate and the biopsy priorities, one can use the cost functions, the algorithm level approaches, ensemble learning or data-level approaches [17]. The latter intends to generate new samples to balance the dataset. In the literature, it is also found some key techniques that are most often used to balance data, such as SMOTE [18], ADASYN [19] and ROSE [20], by introducing synthetic examples by means of interpolation between various positive instances that lie together. Though balancing methods with the proposed one converge in terms of balancing purpose, the latter are suitably employed but while using shallow classifiers, such as support vector machines, k-nearest neighbors, owing to the fact that those are focused on the feature space and these learn from extracted features. Moreover, the resulting samples on the original feature space is limited to the local space owing to the interpolation of the synthetic between the smaller class example processing and one of its nearest neighbors. When the neighbor is far from the center, which means that there are but a small number of examples in the local space near the center and the true underlying distribution of the class will simply be expressed unreliable, which, in the case of HIs, means that new samples will be the approximation of existing samples, not solving the inter-patient diversity nonetheless.

III. PROPOSED METHOD

The proposed method intends to improve the generalization ability of machine learning algorithms dealing with HIs, by considering the inter-patient variability. We propose the use of a blending method to composite images of different patients with the same type of tumor (benign or malignant). The present approach generates a new training image made up by half images of different patients. This strategy aims to avoid that a model learns color representations of patients, which, in fact, are related but to the stain process. While the straightforward blending of two images may produce artifacts owing to the adjacent pixel intensity difference, to remove such artifacts Gaussian-Laplacian Pyramid was used.

A. Gaussian-Laplacian Pyramid (GLP)

In signal processing and computer vision, pyramid representation (Fig. 1(a)) is the main type of multi-scale representation for computing image features in different scales. The pyramid is obtained by repeated smoothing and subsampling of an image or a signal. This concept is frequently used because it expresses computational efficiency approximation compared to other representations such as scale-space representation

$$G_0(x, y) = \begin{cases} I(x, y), & \text{for level, } l = 0 \\ \sum_{m=-2}^2 \sum_{n=-2}^2 w(m, n) G_{l-1}(2x + m, 2y + n), & \text{otherwise.} \end{cases} \quad (1)$$

where $w(m, n)$ is a weighting function (identical at all levels) termed the generating kernel which adheres to the following properties: separable, symmetric and each node at level n contributes the same total weight to nodes at level $l + 1$. The pyramid name arose from the fact that the weighting function nearly approximates a Gaussian function [28]. This pyramid holds local averages on different scales, which has been leveraged for target localization and texture analysis [29]–[31].

In order to seamlessly stitch together image A and image B into an image composite on a scale-dependent way such that to avoid boundary artifacts, the LP (Fig. 1) is used. LP uses GP to blend images by preserving the significant feature meanwhile. The process is performed by downsizing the images into different levels (sizes) with Gaussian. Afterward, the Gaussian is expanded into the lower level and subtracts from the image in that level to acquire the Laplacian image. In other word, a level in LP is formed by the difference between that level in GP and expanded version of its upper level in GP. The smallest level, however, is not a difference image for enabling the high-resolution image reconstruction.

Formally speaking, assuming the GP $[I_0, I_1, \dots, I_k]$, the LP is obtained by computing $b_k = I_k - EI_{k+1}$, where EI_{k+1} represents an up-sampled, smoothed version of I_{k+1} of the same dimension. In the literature, LP is used for image

and multi-resolution analysis [21]–[23]. For generating the pyramid representation, different smoothing kernels have been brought forward and the binomial one strikingly shows up as useful and theoretically well-founded [24], [25].

Accordingly, for a bi-dimensional image, the normalized binomial filter may be applied (1/4, 1/2, 1/4) in most cases twice or even more along all spatial dimensions, afterward, the subsampling of the image by a factor of two, which lead to efficient and compact multi-level representation. There are two main types of pyramids, namely, low-pass and band-pass [26], [27]. In order to develop filter-based representations by decomposing images into information on multiple scales as well as to extract features/structures of interest from an image, Gaussian pyramid (GP), Laplacian Pyramid (LP) and Wavelet pyramid are examples of the most frequently used pyramids.

The GP (Fig. 1) consists of low-pass filtered, reduced density, where subsequent images of the preceding level of the pyramid are weighted down by means of Gaussian average or Gaussian blur and scaled down. The base level is defined as the original image. Formally speaking, assuming that $I(x, y)$ is a two-dimensional image, the GP is recursively defined in (1).

compression, enhancements, analysis and graphics [27].

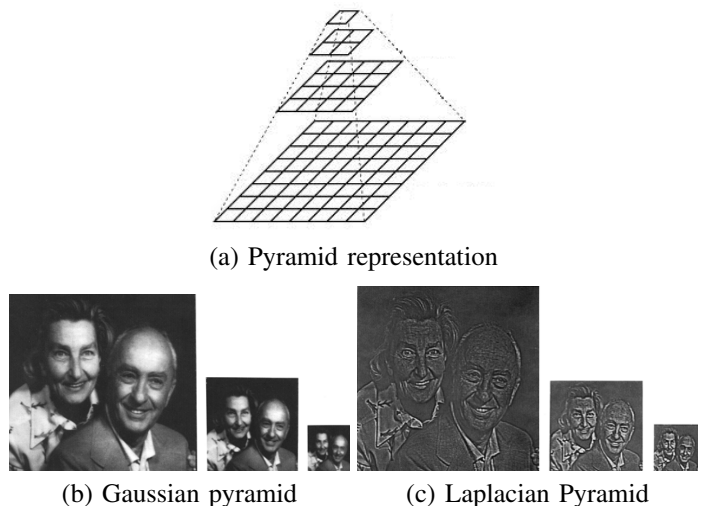


Fig. 1: An example of Gaussian and Laplacian Pyramids from the same input image. (b) First three levels of Gaussian pyramid; (c) First three levels of Laplacian pyramid. Images adapted from [27].

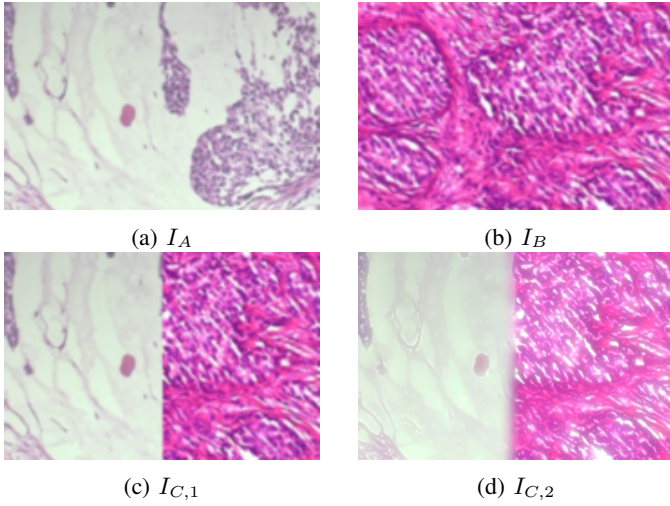


Fig. 2: Example of image blending: (a and b) Two different images to be blended; (c) $I_{C,1}$ is a direct blending of I_A and I_B ; (d) $I_{C,2}$ is a multi-resolution blending of I_A and I_B .

B. Pyramid Blending (PB)

Blending is a common task in several scientific applications and advertising, whose purpose is to join smoothly two images or objects into a larger composite in such a way that their respective boundaries junctions are unnoticed [27]. Fig. 2 shows an example of blending two images.

Let I_A and I_B be two images of the same resolution, and I_C be the composite from blending $I_{A,left}$ and $I_{B,right}$ which are the left and the right half of I_A and I_B , respectively. The direct blending is given by (2).

$$I_C = I_{A,left} + I_{B,right} \quad (2)$$

As shown in Fig. 2(b)-left, I_C is often a composite in which the boundary junction is apparent when splining two images. The transition from one image to the other in case of direct blending may carry mismatch of both low and high frequencies.

C. Proposed Approach for Data Augmentation

This section presents an efficient approach using Gaussian-Laplacian pyramid blending (GLPB) for HI data augmentation. An overview of the proposed approach is shown in Fig. 3:

The proposed approach for data augmentation is based on blending two images of two different patients to generate a third image. As stated in Section III-B, the direct blending of $I_{A,left}$ and $I_{B,right}$ usually carries mismatch of low and high frequencies, therefore the boundary junction is evident and the resulting image does not look natural. Our hypothesis is that pyramid blending stands out as the most suitable solution to address this issue and produce natural-looking HIs. This process consists of decomposing each image into a set spatial-frequency bands. Afterwards, a band-pass composite can be constructed in each band by means of a transition zone. The latter is comparable in width to the wavelength representation

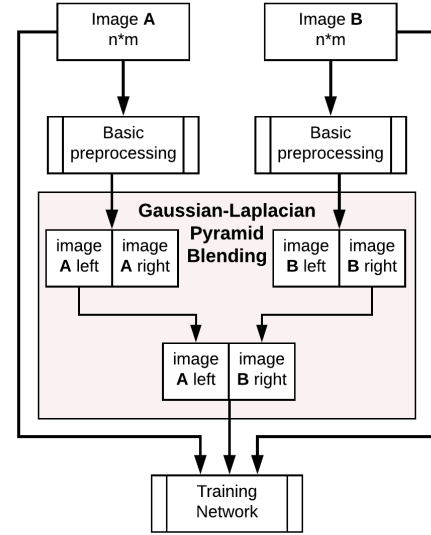


Fig. 3: An overview of the proposed approach for data augmentation based on GLPB.

in the band. To obtain the final composite, component band-pass composites are summed. The computational steps of the proposed multi-resolution splining procedure are quite feasible when pyramid methods are used [27].

In order to stitch together $I_{A,left}$ and $I_{B,right}$ into an image composite with minimum or no apparent junction boundaries, the Laplacian pyramid is used to smoothing the boundary on a scale-dependent way to avoid boundary artifacts. Assuming that I_A and I_B have the same resolution, the proposed approach is made up of the following steps:

- 1) Split I_A and I_B in half left and right;
- 2) Build Laplacian pyramids LA from I_A and LB from I_B
- 3) Build a Gaussian pyramid GR
- 4) Form a combined pyramid LC from LA and LB using nodes of GR as weights:

$$* LC(i, j) = GR(i, j) * LA(i, j) + (1 - GR(i, j)) * LB(i, j)$$

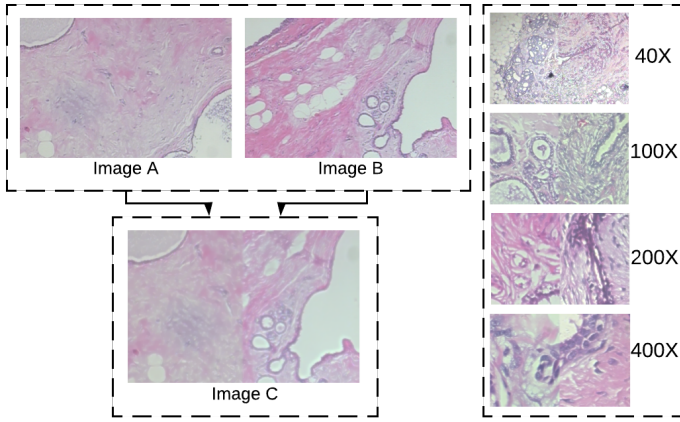
The pyramid LC is constructed for the composite image by setting each node equal to the corresponding node in LA or LB that has the larger absolute value [27].

- 5) Collapse combined pyramid to the reconstruct image

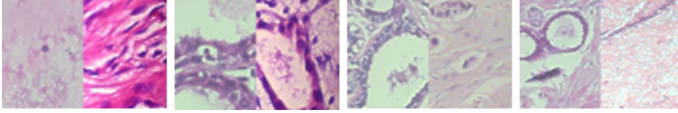
Fig. 4 illustrates the results from the methodology hereof with HIs from BreakHis dataset [32].

IV. EXPERIMENTAL SETUP

The dataset used in the experiments is the BreakHis [32]. It consists of 7,909 breast cancer histopathologic images. The images are labeled following eight types of tumor, four malignant and four benign. The distribution of images is imbalanced according to the tumor type, due to the prevalence of certain tumor types in the population, presented in Table II.



(a) Image blending with pyramids (left), examples of blending in which the stitching not evident (right).



(b) Examples of blending results in which the stitching is evident.

Fig. 4: Example of histopathological images blending: (a) Image C is the composite of the pyramid blending of Image A and Image B; images on the right side are generated composites (generated images) from pyramid blending of different patients. Each image is the result of different images of different magnitudes such as 40 \times , 100 \times , 200 \times and 400 \times as specified on the right side of each image. The original and generated images are used together to train the network; (b) samples whose blending process presents artifacts.

The original image size is 700 \times 460 pixels and 8-bits RGB. We used images downsized by half to reduce the CNN overhead. The classification considered but benign and malignant classes, that is, all benign tumors are considered as a single class and all malignant tumor as another class.

HIs do not have a defined geometric structure like macroscopic images do, thus, we use a compact CNN model [33], named Texture CNN (TCNN). The network architecture is presented in Table I and it consists of two convolutional layers interleaved with batch normalization layers, a global average pooling, and two fully connected layers. All layers except the last one use ReLU activation function. The implementation was done using Pytorch version 1.1.0. We used adadelata for optimization with learning rate of 0.1 and 25 epochs. The number of images used in the experiments is reduced, taking into account that the 7,909 images are divided into four magnification factors. This is the other reason for employing TCNN, which has fewer parameters compared to other CNN architectures such as VGG or ResNet.

We analyzed the impact of data augmentation on TCNN by varying the augmentation factor. A interesting analysis regarding data augmentation and TCNN can be found in [34],

which used an approach based on the color information [35]. It applies a variable random hue, bright and contrast maximum alteration of 4%, 25% and 25%, respectively. The color augmentation procedure can also work as a color normalization, reducing the bias of stain alterations.

TABLE I: The architecture of TCNN.

Layer	Size	Kernel	Filters
Input	350 \times 230	-	3
Conv2D	350 \times 230	3	32
BatchNorm	350 \times 230	-	-
ReLU	350 \times 230	-	-
Conv2D	350 \times 230	3	32
BatchNorm	350 \times 230	-	-
ReLU	350 \times 230	-	-
GlobalAveragePool	1 \times 1	-	32
FullyConnected	32	-	-
ReLU	32	-	-
FullyConnected	16	-	-
SoftMax	2	-	-

TABLE II: Image and patient distribution in BreakHis dataset.

Tissue Type	Tumor Type	# of Images	# of Patients
Benign	Adenosis	444	4
	Fibroadenoma	1,014	10
	Phyllodes tumor	453	3
	Tubular adenoma	569	7
	Total	2,368	24
Malign	Ductal carcinoma	3,451	38
	Lobular carcinoma	626	5
	Mucinous carcinoma	792	9
	Papillary carcinoma	560	6
	Total	5,429	58

It is worthy of note that the comparisons herein are more focused on the imbalance problem of the dataset, meaning that we used the GLPB to generate but new images of the benign type of tumor. We have not applied the GLPB in the malignant images. We generated as many benign images as necessary to equalize the amount of benign and malignant images. The GLPB approach was evaluated using no data augmentation (GLPB), using additional color data augmentation over the entire set of equalized images (benign and malignant) to double the training set (GLPB 2 \times) and to augment it six times (GLPB 6 \times). So, all experiments with GLPB were based in the GLPB equalized dataset.

Furthermore, we have also implemented a blending algorithm to minimize the boundary junction formed between the combination of the two images after a direct blending. This blending (Mix) applies a color linear combination in the middle of the combined images (half of each image), resulting in a smooth transition between them. We applied the Mix between benign random images (Mix B&M) and we also mixed images of the same sub-type of tumor, e.g. adenoma images of two different patients (Mix Subtype). We also compared our results with the original dataset, that is, the dataset with neither data augmentation nor balancing (No Aug). Furthermore, the classification results without balancing, but using only color data augmentation are also presented. All data augmentation procedures (blending and color data augmentation) were applied only to the training set.

In addition, we have also used an approach based on Generative Adversarial Network (GAN) to generate a combination of images between patients. We used the same network proposed by [36], called CycleGAN, which generates new images combining features from two origins. We combined the same images used in the GLPB approach with the intention of balancing the dataset and also applied $2\times$ and $6\times$ data augmentation.

In total we have carried out 10 experiments, three involving the GLPB approach, three with GAN balanced dataset, two with no balancing and two using the Mix approach. All experiments were repeated five times according to the experimental setup proposed by [32], which is a five-fold repeated holdout. The proportion of training/test data is 70%/30% patient-wise respectively, which means that no patient has parts of her images in training or test simultaneously. Another important aspect of the experiments is that we did not mix images of different magnifications. As a result of the experiment setup, we performed 200 executions. .

V. RESULTS AND DISCUSSION

The experiment results are summarized in Table III. Our results are reported following image-level and patient-level. For image-level, we also present the balanced accuracy, which in this two-class problem is the mean of specificity and sensitivity. All results are the mean of the five folds followed by their standard deviation. Our approach performed better than other methods compared with $400\times$ and $200\times$. We can also highlight the result for Aug $2\times$ and $200\times$ where the patient’s accuracy is high, close to our method, but when looking at the balanced accuracy, it does not present good balanced image-level accuracy. In other words, it only performed well in one class, which shows the importance of presenting the balanced accuracy due to the dataset imbalance. The approaches of mixing images, both by GLPB and *Mix* presented good results with a small advantage margin to GLPB.

It is remarkable that $200\times$ is the most significant result for our proposal, presenting the best accuracy (image, image balanced and patient accuracy). Comparing these results to the ones reported in some state-of-the-art results (Table IV) it outperformed them. We included in Table IV only results that followed the same fold distribution. Other results can be found in [37], with better results, but using other fold distribution. The baseline results are based on handcrafted feature extractors for texture and obtained better results with $200\times$. AlexNet and Deep features are CNN based and present better results in $100\times$ and $40\times$. Our approach used a small CNN, designed for texture recognition, which also presented good results for $200\times$.

We present in Fig. 5 an example of HIs of two tumor types with two different magnifications. Figs. 5a and 5b are Ductal Carcinoma images of $40\times$ and $400\times$. Figs. 5a and 5b are Adenoma images of $40\times$ and $400\times$ magnification factors. These images highlight the differences in the objective into which the filters are trained. In the $40\times$ magnification it is difficult to identify nucleus pleomorphism since they

TABLE III: Five-fold mean image-level accuracy, image-level balanced accuracy and patient-level accuracy for four magnification factors. In bold, the best values

Method	Magnification				
	$400\times$	$200\times$	$100\times$	$40\times$	
Image	GLPB	0.872 ± 0.045	0.884 ± 0.050	0.814 ± 0.048	0.821 ± 0.064
	GLPB $2\times$	0.851 ± 0.061	0.884 ± 0.058	0.830 ± 0.057	0.808 ± 0.071
	GLPB $6\times$	0.837 ± 0.037	0.876 ± 0.049	0.823 ± 0.046	0.787 ± 0.054
	Mix B&M	0.871 ± 0.050	0.883 ± 0.050	0.824 ± 0.045	0.841 ± 0.055
	Mix Subtype	0.821 ± 0.065	0.874 ± 0.059	0.822 ± 0.055	0.803 ± 0.065
	No Aug	0.692 ± 0.067	0.816 ± 0.063	0.698 ± 0.026	0.678 ± 0.034
	Aug $2\times$	0.798 ± 0.064	0.874 ± 0.040	0.771 ± 0.011	0.745 ± 0.063
	GAN	0.851 ± 0.050	0.870 ± 0.056	0.804 ± 0.042	0.774 ± 0.085
	GAN $2\times$	0.849 ± 0.057	0.874 ± 0.057	0.821 ± 0.032	0.805 ± 0.067
	GAN $6\times$	0.839 ± 0.041	0.877 ± 0.049	0.813 ± 0.021	0.795 ± 0.049
Balanced	GLPB	0.847 ± 0.043	0.875 ± 0.063	0.795 ± 0.044	0.803 ± 0.049
	GLPB $2\times$	0.845 ± 0.056	0.878 ± 0.068	0.821 ± 0.064	0.808 ± 0.069
	GLPB $6\times$	0.831 ± 0.033	0.868 ± 0.062	0.820 ± 0.047	0.795 ± 0.051
	Mix B&M	0.846 ± 0.051	0.866 ± 0.065	0.793 ± 0.064	0.807 ± 0.065
	Mix Subtype	0.818 ± 0.063	0.861 ± 0.069	0.793 ± 0.063	0.792 ± 0.074
	No Aug	0.547 ± 0.073	0.720 ± 0.073	0.543 ± 0.030	0.513 ± 0.026
	Aug $2\times$	0.711 ± 0.087	0.819 ± 0.053	0.661 ± 0.010	0.617 ± 0.095
	GAN	0.816 ± 0.057	0.847 ± 0.064	0.763 ± 0.043	0.709 ± 0.129
	GAN $2\times$	0.834 ± 0.052	0.853 ± 0.063	0.788 ± 0.038	0.769 ± 0.061
	GAN $6\times$	0.821 ± 0.033	0.855 ± 0.050	0.768 ± 0.026	0.761 ± 0.056
Patient	GLPB	0.882 ± 0.043	0.896 ± 0.054	0.835 ± 0.022	0.845 ± 0.042
	GLPB $2\times$	0.857 ± 0.061	0.891 ± 0.067	0.852 ± 0.047	0.825 ± 0.067
	GLPB $6\times$	0.847 ± 0.032	0.887 ± 0.055	0.841 ± 0.048	0.789 ± 0.063
	Mix B&M	0.877 ± 0.053	0.890 ± 0.056	0.835 ± 0.029	0.860 ± 0.049
	Mix Subtype	0.823 ± 0.053	0.885 ± 0.063	0.834 ± 0.044	0.826 ± 0.059
	No Aug	0.711 ± 0.054	0.830 ± 0.053	0.708 ± 0.025	0.689 ± 0.022
	Aug $2\times$	0.815 ± 0.066	0.891 ± 0.035	0.771 ± 0.021	0.755 ± 0.066
	GAN	0.856 ± 0.053	0.884 ± 0.056	0.813 ± 0.046	0.796 ± 0.073
	GAN $2\times$	0.857 ± 0.062	0.883 ± 0.062	0.842 ± 0.025	0.825 ± 0.057
	GAN $6\times$	0.850 ± 0.047	0.886 ± 0.055	0.835 ± 0.023	0.814 ± 0.043

are too small. On the other hand, this magnification makes easy to detect forms like the ones that characterize papillary carcinoma. The characteristics of magnifications impact in the network used, taking into account that the small network does not have the capabilities of large objects recognizing, only textures.

To the same extent, future work studies may include shallow methods in order to compare the performance of GLPB vis-à-vis other techniques of undersampling and oversampling such as SMOTE and NearMiss algorithms.

TABLE IV: State-of-the-art patient accuracy results with the same fold split.

Method	Magnification			
	$400\times$	$200\times$	$100\times$	$40\times$
Baseline [32]	0.823 ± 0.038	0.851 ± 0.031	0.821 ± 0.049	0.838 ± 0.041
AlexNet [13]	0.817 ± 0.049	0.853 ± 0.038	0.845 ± 0.024	0.886 ± 0.056
Deep Features [38]	0.861 ± 0.062	0.863 ± 0.035	0.884 ± 0.048	0.840 ± 0.069
Mi [39]	0.827 ± 0.030	0.872 ± 0.043	0.891 ± 0.052	0.921 ± 0.059
GLPB	0.882 ± 0.043	0.896 ± 0.054	0.835 ± 0.022	0.845 ± 0.042

We present in Table V the subclass classification result for $40\times$ and $200\times$ magnification using GLPB $2\times$. These are the two scenarios where GLPB obtained the worst and best results. We consider $40\times$ the worst result because the difference to the state-of-the-art is the highest one. We also show the Aug $2\times$

TABLE V: Classification results considering subclass distribution for 40 \times and 200 \times using GLPB 2 \times and 200 \times with Aug 2 \times . Adenoma (A), Fibroadenoma (F), Tubular Adenoma (TA), Phyllodes Tumor (PT), Ductal Carcinoma (DC), Papillary Carcinoma (PC), Mucinous Carcinoma (MC) and Lobular Carcinoma (LC)

		Predicted									
		B	M	B	M	B	M	B	M		
		Mag 40\times GLPB 2\times									
Benign	A	0.71	0.29	0.68	0.32	1.00	0.00	1.00	0.00	0.88	0.13
	F	0.91	0.09	0.85	0.15	0.77	0.23	0.75	0.25	0.78	0.22
	TA	0.73	0.27	0.56	0.44	1.00	0.00	0.48	0.52	0.51	0.49
	PT	0.74	0.26	1.00	0.00	1.00	0.00	1.00	0.00	0.55	0.45
Malignant	DC	0.12	0.88	0.08	0.92	0.10	0.90	0.23	0.77	0.05	0.95
	PC	0.62	0.38	0.75	0.25	0.11	0.89	0.69	0.31	0.18	0.82
	MC	0.13	0.87	0.40	0.60	0.11	0.89	0.44	0.56	0.07	0.93
	LC	0.11	0.89	0.07	0.93	0.00	1.00	0.04	0.96	0.00	1.00
		Mag 200\times GLPB 2\times									
Benign	A	0.81	0.19	0.56	0.44	0.98	0.02	0.98	0.02	0.96	0.04
	F	0.98	0.02	1.00	0.00	1.00	0.00	0.72	0.28	0.97	0.03
	TA	0.86	0.14	0.55	0.45	1.00	0.00	0.58	0.42	0.90	0.10
	PT	0.75	0.25	0.93	0.07	0.93	0.07	1.00	0.00	0.78	0.22
Malignant	DC	0.09	0.91	0.05	0.95	0.07	0.93	0.11	0.89	0.05	0.95
	PC	0.32	0.68	0.69	0.31	0.00	1.00	0.47	0.53	0.02	0.98
	MC	0.05	0.95	0.15	0.85	0.02	0.98	0.42	0.58	0.12	0.88
	LC	0.09	0.91	0.00	1.00	0.00	1.00	0.00	1.00	0.00	1.00
		Mag 200\times Aug 2\times									
Benign	A	0.40	0.60	0.42	0.58	0.66	0.34	0.65	0.35	0.63	0.37
	F	0.82	0.18	1.00	0.00	0.98	0.02	0.71	0.29	0.66	0.34
	TA	0.49	0.51	0.55	0.45	0.90	0.10	0.51	0.49	0.46	0.54
	PT	0.54	0.46	0.79	0.21	0.71	0.29	0.76	0.24	0.54	0.46
Malignant	DC	0.01	0.99	0.02	0.98	0.01	0.99	0.01	0.99	0.00	1.00
	PC	0.11	0.89	0.54	0.46	0.00	1.00	0.06	0.94	0.00	1.00
	MC	0.00	1.00	0.04	0.96	0.00	1.00	0.04	0.96	0.01	0.99
	LC	0.01	0.99	0.00	1.00	0.00	1.00	0.00	1.00	0.00	1.00

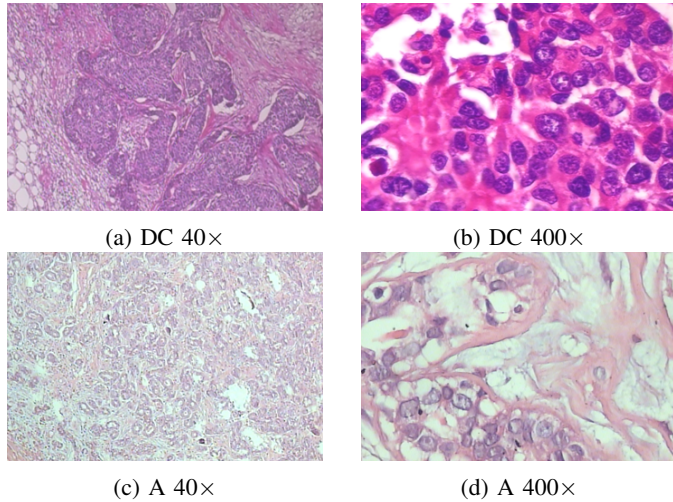


Fig. 5: Comparison of Ductal Carcinoma (DC) and Adenoma (A) images with magnification of (a) 40 \times (b) 400 \times (c) 40 \times (d) 400 \times

result for 200 \times that obtained good patient accuracy results but presented poor balanced accuracy results. It can be seen in Table V, where the Malignant tumors were much better identified than the Benign.

VI. CONCLUSION

The work herein presents a noteworthy methodology regarding the use of Gaussian and Laplacian pyramids methods concerning data augmentation. We investigated how the classifiers can be improved in terms of the generalization ability considering the inter patient variability. We stated that a data augmentation could be decomposed into image blending such that from two images the third can be generated, where each one is of a different patient, while producing both a balanced dataset and good classification accuracy, precision and recall.

It is essential to consider that Gaussian-Laplacian pyramids provide a powerful mathematical tool for representing multi-resolutions of an image as well as a blending between two images of the same class while finding a most favorable seam and avoiding artifacts along boundaries. Thence, in this paper, blending images helped to augment the database and to balance the respective classes under investigation, meanwhile performing at comparable accuracy as other state-of-the-art methods. The blending method can provide improvements on the results of the other state-of-the-art methods, considering that it works in the data preprocessing and can be allied with the reported literature best methods. Accordingly, this methodology is promising to befit data limitation problems, in particular where the classification regards the HI as a whole image, not using patches.

REFERENCES

- [1] F. Bray, J. Ferlay, I. Soerjomataram, R. L. Siegel, L. A. Torre, and A. Jemal, "Global cancer statistics 2018: GLOBOCAN estimates of incidence and mortality worldwide for 36 cancers in 185 countries," *CA: A Cancer Journal for Clinicians*, vol. 68, no. 6, pp. 394–424, 2018.
- [2] L. A. Torre, F. Islami, R. L. Siegel, E. M. Ward, and A. Jemal, "Global cancer in women: Burden and trends," *Cancer Epidemiology and Prevention Biomarkers*, vol. 26, no. 4, pp. 444–457, 2017.
- [3] Anger E. Flejou J.-F. Galateau F. Gaulard P. Guiu M. Michiels J.-F. Saint-Andre J.-P. Scoazec J.Y. Vacher-Lavenu M.-C. Camparo P. Capron F. Chenard M.-P. Chetritt J. Chigot J.-P. Cochand-Priollet B.; Coindre J.-M. Copin M.-C. Belloq, J.-P., "Sécuriser le diagnostic en anatomie et cytologie pathologiques en 2011. l'erreur diagnostique: entre discours et réalité," in *Annales de pathologie*, 2011.
- [4] J de Matos, A. de Souza Britto Jr., L. E. S. Oliveira, and A. L. Koerich, "Histopathologic image processing: A review," *CoRR*, vol. abs/1904.07900, 2019.
- [5] B. Ehteshami Bejnordi, G. Litjens, N. Timofeeva, I. Otte-Höller, A. Homeyer, N. Karssemeijer, and J. A. van der Laak, "Stain specific standardization of whole-slide histopathological images," *IEEE Transactions on Medical Imaging*, vol. 35, no. 2, pp. 404–415, Feb 2016.
- [6] F. Ciompi, O. Geessink, B. E. Bejnordi, G. S. de Souza, A. Baidoshvili, G. Litjens, B. van Ginneken, I. Nagtegaal, and J. van der Laak, "The importance of stain normalization in colorectal tissue classification with convolutional networks," in *IEEE 14th International Symposium on Biomedical Imaging (ISBI)*, April 2017, pp. 160–163.
- [7] J. Deng, W. Dong, R. Socher, L.-J. Li, K. Li, and L. Fei-Fei, "ImageNet: A Large-Scale Hierarchical Image Database," in *The IEEE Conference on Computer Vision and Pattern Recognition (CVPR)*, 2009.
- [8] G. Zhang, M. Xiao, and Y.-H. Huang, "Histopathological image recognition with domain knowledge based deep features," in *Intelligent Computing Methodologies*, D.-S. Huang, M. M. Gromiha, K. Han, and A. Hussain, Eds., Cham, 2018, pp. 349–359, Springer International Publishing.
- [9] V. Gupta and A. Bhavsar, "Sequential modeling of deep features for breast cancer histopathological image classification," in *The IEEE Conference on Computer Vision and Pattern Recognition (CVPR) Workshops*, June 2018.

- [10] Z. Gandomkar, P. C. Brennan, and C. Mello-Thoms, "Mudern: Multi-category classification of breast histopathological image using deep residual networks," *Artificial Intelligence in Medicine*, vol. 88, pp. 14–24, 2018.
- [11] D. Bardou, K. Zhang, and S. M. Ahmad, "Classification of breast cancer based on histology images using convolutional neural networks," *IEEE Access*, vol. 6, pp. 24680–24693, 2018.
- [12] K. Roy, D. Banik, D. Bhattacharjee, and M. Nasipuri, "Patch-based system for classification of breast histology images using deep learning," *Computerized Medical Imaging and Graphics*, vol. 71, pp. 90–103, 2019.
- [13] F. A. Spanhol, L. S. Oliveira, C. Petitjean, and L. Heutte, "Breast cancer histopathological image classification using convolutional neural networks," in *International Joint Conference on Neural Networks (IJCNN)*, July 2016, pp. 2560–2567.
- [14] J. de Matos, A. de Souza Britto Jr., L. E. S. Oliveira, and A. L. Koerich, "Double transfer learning for breast cancer histopathologic image classification," in *International Joint Conference on Neural Networks, IJCNN*, 2019, pp. 1–8.
- [15] M. W. Lafarge, J. P. W. Pluim, K. A. J. Eppenhof, P. Moeskops, and M. Veta, "Domain-adversarial neural networks to address the appearance variability of histopathology images," in *Deep Learning in Medical Image Analysis and Multimodal Learning for Clinical Decision Support*, M. J. Cardoso, T. Arbel, G. Carneiro, T. Syeda-Mahmood, J. M. R. S. Tavares, M. Moradi, A. Bradley, H. Greenspan, J. P. Papa, A. Madabhushi, J. C. Nascimento, J. S. Cardoso, V. Belagiannis, and Z. Lu, Eds., Cham, 2017, pp. 83–91, Springer International Publishing.
- [16] H. Lin, H. Chen, Q. Dou, L. Wang, J. Qin, and P. Heng, "Scannet: A fast and dense scanning framework for metastatic breast cancer detection from whole-slide image," in *IEEE Winter Conference on Applications of Computer Vision (WACV)*, March 2018, pp. 539–546.
- [17] A. Fernandez, S. Garca, M. Galar, R. C. Prati, B. Krawczyk, and F. Herrera, *Learning from Imbalanced Data Sets*, Springer Publishing Company, Incorporated, 1st edition, 2018.
- [18] N. V. Chawla, K. W. Bowyer, L. O. Hall, and W. P. Kegelmeyer, "Smote: synthetic minority over-sampling technique," *Journal of artificial intelligence research*, vol. 16, pp. 321–357, 2002.
- [19] H. He, Y. Bai, E. A. Garcia, and S. Li, "Adasyn: Adaptive synthetic sampling approach for imbalanced learning," in *IEEE international joint conference on neural networks*. IEEE, 2008, pp. 1322–1328.
- [20] G. Menardi and N. Torelli, "Training and assessing classification rules with imbalanced data," *Data Mining and Knowledge Discovery*, vol. 28, no. 1, pp. 92–122, 2014.
- [21] J. L. Crowley and O. Riff, "Fast computation of scale normalised gaussian receptive fields," in *International Conference on Scale-Space Theories in Computer Vision*. Springer, 2003, pp. 584–598.
- [22] D. G. Lowe, "Distinctive image features from scale-invariant keypoints," *International journal of computer vision*, vol. 60, no. 2, pp. 91–110, 2004.
- [23] P. J. Burt, "Fast filter transform for image processing," *Computer graphics and image processing*, vol. 16, no. 1, pp. 20–51, 1981.
- [24] T. Lindeberg, *Scale-space theory in computer vision*, vol. 256, Springer Science & Business Media, 2013.
- [25] J. L. Crowley, "A representation for visual information.," Tech. Rep., Carnegie-Mellon University, 1981.
- [26] P. Burt and E. Adelson, "The laplacian pyramid as a compact image code," *IEEE Transactions on communications*, vol. 31, no. 4, pp. 532–540, 1983.
- [27] E. H. Adelson, C. H. Anderson, J. R. Bergen, P. J. Burt, and J. M. Ogden, "Pyramid methods in image processing," *RCA engineer*, vol. 29, no. 6, pp. 33–41, 1984.
- [28] K. G. Derpanis, "The gaussian pyramid," 2005.
- [29] P. J. Burt, "Fast algorithms for estimating local image properties," *Computer Vision, Graphics, and Image Processing*, vol. 21, no. 3, pp. 368–382, 1983.
- [30] L. I. Larkin and P. J. Burt, "Multi-resolution texture energy measures," in *Proceedings in IEEE conference on computer vision and pattern recognition*, 1983.
- [31] C. H. Anderson, P. J. Burt, and G. S. Van Der Wal, "Change detection and tracking using pyramid transform techniques," in *Intelligent Robots and Computer Vision IV*. International Society for Optics and Photonics, 1985, vol. 579, pp. 72–78.
- [32] F. A. Spanhol, L. S. Oliveira, C. Petitjean, and L. Heutte, "A dataset for breast cancer histopathological image classification," *IEEE Transactions on Biomedical Engineering*, vol. 63, no. 7, pp. 1455–1462, July 2016.
- [33] V. Andrearczyk and P. F. Whelan, "Using filter banks in convolutional neural networks for texture classification," *Pattern Recognition Letters*, vol. 84, pp. 63–69, 2016.
- [34] J. de Matos, A. de Souza Britto, L. E. S. de Oliveira, and A. L. Koerich, "Texture cnn for histopathological image classification," in *2019 IEEE 32nd International Symposium on Computer-Based Medical Systems (CBMS)*, June 2019, pp. 580–583.
- [35] D. Tellez, M. Balkenhol, I. Otte-Höller, R. van de Loo, R. Vogels, P. Bult, C. Wauters, W. Vreuls, S. Mol, N. Karssemeijer, G. Litjens, J. van der Laak, and F. Ciompi, "Whole-slide mitosis detection in h e breast histology using phh3 as a reference to train distilled stain-invariant convolutional networks," *IEEE Transactions on Medical Imaging*, vol. 37, no. 9, pp. 2126–2136, Sep. 2018.
- [36] J. Zhu, T. Park, P. Isola, and A. A. Efros, "Unpaired image-to-image translation using cycle-consistent adversarial networks," in *IEEE International Conference on Computer Vision (ICCV)*, Oct 2017, pp. 2242–2251.
- [37] Y. Benhammou, B. Achchab, F. Herrera, and S. Tabik, "Breakhis based breast cancer automatic diagnosis using deep learning: Taxonomy, survey and insights," *Neurocomputing*, vol. 375, pp. 9–24, 2020.
- [38] F. A. Spanhol, L. S. Oliveira, P. R. Cavalin, C. Petitjean, and L. Heutte, "Deep features for breast cancer histopathological image classification," in *IEEE International Conference on Systems, Man, and Cybernetics (SMC)*, Oct 2017, pp. 1868–1873.
- [39] P. J. Sudharshan, C. Petitjean, F. Spanhol, L. E. Oliveira, L. Heutte, and P. Honeine, "Multiple instance learning for histopathological breast cancer image classification," *Expert Systems with Applications*, vol. 117, pp. 103–111, 2019.